remote sensing

MDPI

Article

Monitoring Braided River-Bed Dynamics at the Sub-Event Time Scale Using Time Series of Sentinel-1 SAR Imagery

Daniele Rossi *,†, Guido Zolezzi ‡, Walter Bertoldi ‡ and Alfonso Vitti ‡

Department of Civil, Environmental and Mechanical Engineering, University of Trento, Via Mesiano 77, 38123 Trento, Italy; guido.zolezzi@unitn.it (G.Z.); walter.bertoldi@unitn.it (W.B.); alfonso.vitti@unitn.it (A.V.)

* Correspondence: daniele.rossi@unitn.it

† Current address: Easter Alps River Basin District, Piazza A. Vittoria 5, 38122 Trento, Italy.

‡ These authors contributed equally to this work.

Abstract: Remote sensing plays a central role in the assessment of environmental phenomena and has increasingly become a powerful tool for monitoring shorelines, river morphology, flood-wave delineation and flood assessment. Optical-based monitoring and the characterization of river evolution at long time scales is a key tool in fluvial geomorphology. However, the evolution occurring during extreme events is crucial for the understanding of the river dynamics under severe flow conditions and requires the processing of data from active sensors to overcome cloud obstructions. This work proposes a cloud-based unsupervised algorithm for the intra-event monitoring of river dynamics during extreme flow conditions based on the time series of Sentinel-1 SAR data. The method allows the extraction of multi-temporal series of spatially explicit geometric parameters at high temporal and spatial resolutions, linking them to the hydrometric levels acquired by reference gauge stations. The intra-event reconstruction of inundation dynamics has led to (1) the estimation of the relationship between hydrometric level and wet area extension and (2) the assessment of bank erosion phenomena. In the first case, the behavior exhibits a change when the hydrometric level exceeds 1 m. In the second case, the erosion rate and cumulative lateral erosion were evaluated. The maximum erosion velocity was greater than 1 m/h, while the cumulative lateral erosion reached 130 m. Time series of SAR acquisitions, provided by Sentinel-1 satellites, were analyzed to quantify changes in the wet area of a reach of the Tagliamento river under different flow conditions. The algorithm, developed within the Python-API of GEE, can support many types of analyses of river dynamics, including morphological changes, floods monitoring, and bio-physical habitat dynamics. The results encourage future advancements and applications of the algorithm, specifically exploring SAR data from ICEYE and Capella Space constellations, which offer significantly higher spatial and temporal resolutions compared to Sentinel-1 data.

Keywords: SAR; gravel-bed rivers; morphodynamics; flood dynamics; river bank erosion

Citation: Rossi, D.; Zolezzi, G.; Bertoldi, W.; Vitti, A. Monitoring Braided River-Bed Dynamics at the Sub-Event Time Scale Using Time Series of Sentinel-1 SAR Imagery. *Remote Sens.* **2023**, *15*, 3622. https://doi.org/10.3390/rs15143622

Academic Editors: Michael Nones, Paolo Paron and Maria Nicolina Papa

Received: 1 June 2023
Revised: 18 July 2023
Accepted: 18 July 2023
Published: 20 July 2023

1. Introduction

Rivers and their floodplains are among the most complex, dynamic, and diverse ecosystems on Earth, providing major economic, health, cultural, scientific, and educational ecosystem services [1,2]. Despite accounting for just 1.4% of the land surface area, riparian zones provide at least 25% of all terrestrial ecosystem services [3]. Rivers' dynamic behavior originates from the continuous interaction between variable flow, sediment transport and associated morphological change, and ecological feedback, mainly through aquatic and riparian vegetation [4–6]. Most of these dynamic processes occur during floods, which are characterized by the increase in flowing discharge, often associated with a large widening of the inundated areas, both inside the active channel and in adjacent zones. The possibility of understanding, quantifying, and predicting river evolution strongly depends on our ability to monitor what happens during these events, which in some cases last for only a

few hours or days but can shape the riverbed morphology for the following months and years [7,8]. The accurate monitoring of the dynamics of rivers and floodplains plays a vital role in improving river management practices and achieving the objectives outlined in the Water Framework and Flood Directives at the European level (2000/60/EC [9] and 2007/60/EC [10]). Moreover, these directives promote the development of proper flood forecasting and monitoring systems, aiming at preventing high socio-economical losses and at planning a variety of flood-management alternatives [11]. Recent studies have demonstrated that estimation of rainfall provided from the Integrated Multi-satellite Retrievals (IMERG) algorithm for the Global Precipitation Measurement constellation coupled with the mesoscale Weather Research Forecasting (WRF) model [12] can be effectively utilized to accomplish these objectives and fulfill the requirements of the directives [13].

In the last decade, advances in remote sensing technologies and the computational ability to process vast datasets are increasing at unprecedented speed and have revolutionized the way we quantify and assess river systems [14], offering new sources of high resolution, multidimensional data across wide spatial scales and at multiple time scales, towards a data-rich geomorphological science [15]. The availability of different satellite imagery, often freely accessible, can be coupled with various cloud computing platforms and distributed systems such as Google Earth Engine (GEE), Sentinel Hub, Open Data Cube, openEO, and others [16].

Satellite images, and in particular the freely available Landsat and Sentinel-2 multispectral images, have been successfully used for river mapping since the 1990s [17], with continuous improvements since then, towards the accurate evaluation of channel width [18], river centerline and sinuosity [19], and, more in general, for mapping surface water extent and dynamics [20–22].

However, approaches based on optical data in the visible and near-infrared range suffer from strong limitations due to the adverse atmospheric conditions that often characterize flood events. Particularly in the case of relatively small catchments (areas smaller than 10^4–10^5 km^2), flood peaks occur shortly after rain events, implying that cloud coverage is very likely to persist, reducing the possibility of effectively monitoring large river areas. On the contrary, satellites carrying active radar sensors operating in the microwave range are not affected by cloud coverage and therefore provide an attractive way to remotely track the dynamics of rapidly changing river systems. Indeed, Synthetic Aperture Radar (SAR) has played a crucial role in identifying wet and dry classes due to its ability to provide data regardless of the weather conditions or time of observation. Numerous techniques have been developed to fully exploit the potential of SAR data. In the early studies, flood stage measurement, braided river patterns, and river discharge were manually performed by the operator [23–25]. More recently, flood monitoring and river morphology assessments are performed by employing the RGB composition of a reference image (e.g., pre-flood) and a target image (e.g., post-flood), followed by a threshold technique such as the seed-growing segmentation, Maximum Likelihood, or K-means [26–31]. Morphological operators (opening and closing), followed by a K-means thresholding algorithm and a fuzzy logic classifier have been successfully applied to map flooded vegetation [32] and distinguish water surfaces from artifacts caused by heavy precipitation or wet snow [33]. Opening and closing operators, coupled with Support Vector Machine (SVM) [34] and watershed by immersion segmentation [35], are employed, respectively, for extracting river linear features and segmenting the river channel.

However, the application to SAR datasets of fully automated thresholding algorithms, such as the one proposed by Otsu, are still challenging for the scientific community [36,37]. For example, the target class often covers only a small portion of the overall scene, failing to clearly emerge in the histogram of the entire image. Under these circumstances, parametric methods, which typically necessitate the estimation of probability distribution functions for the two target objects (dry soil and wet area, in our case), are not feasible. In this context, several techniques of image splitting and sub-image bimodality testing come into play [38–41].

In the last decade, numerous studies have focused on extracting water streams and water bodies using various approaches that utilize deep neural networks [42–47]. A more detailed description of the aforementioned papers is provided in Section 2.
To improve the efficacy of these methods, in this work, we present the development of an unsupervised and cloud-based algorithm for the near-real-time analysis of stack SAR images. In the workflow, which is described in detail in Section 3, we accomplish the following objectives:

(i) We incorporate water flow level information through metadata enrichment to facilitate the automatic extraction and monitoring of inundation dynamics at a sub-event temporal scale;
(ii) We evaluate the denoising of speckle using three edge-stopping functions; and
(iii) We apply a Self-Adaptive Thresholding Approach (SATA) based on the Otsu Algorithm.

The algorithm is then tested and verified on a 13 km long reach of the Tagliamento River (Italy), a large, braided gravel bed river, recognized as the most natural and dynamic large river in the European Alps. Furthermore, the availability of imagery at the sub-event time scale, as opposed to the standard before–after-flood approach, allows the observation and quantification of lateral bank erosion and channel dynamics during the flood event and with accurate timing as a function of water level and inundation duration.

The paper is organized as follows: Section 2 contains a review of the existing methods that allow river-channel segmentation based on SAR data; Section 3 presents the theoretical approach and describes the details of the computation steps and the dataset; Section 4 illustrates the case study, and Section 5 shows the results of mapping river-inundated areas and morphological change during the flood events that occurred from 2018 to 2020. Discussion on perspectives and limitations of the present work, along with the geomorphological significance and main concluding remarks, is provided in Section 6.

2. Related Works

The detection of flood areas, the extraction of water surfaces, and the monitoring of river morphology have a lowest common denominator: the accurate clustering of images. In the existing literature, different approaches can be found, whose complexity also depends on the historical moment in which the research was conducted.

Brakenridge et al. (1994) [23] and Smith et al. (1995) [24] employed a fixed threshold value for clustering ERS-1 imagery. Brakenridge et al. quantified the flood stage by establishing a correlation between the extent of the 1993 flood of the Mississippi River and high-quality topographic data. On the other hand, Smith et al. examined the correlation between multitemporal surface area of water water and discharge measurements for a braided glacial river in British Columbia.

Nykanen et al. (1998) [25] classified the connected braided system by first manually selecting the upstream part of a known channel and then selecting the disconnected sections that visually appeared to be part of active channels. After approximately one hour of image reworking, the binary classification was completed. They also attempted to use an Unsupervised Bayesian Classification algorithm in order to fully automate the procedure, but the result was a poorly connected braided channel network.

More recently, Klemenjak et al. [34] presented an algorithm for the automatic extraction of river networks that can be applied to multi-temporal or multi-polarized high-resolution SAR data (TerraSAR-X). The method is implemented using the Support Vector Machine and is based on the supervised classification of morphological profiles. They found that in the presence of bridges or power lines the procedure could produce gaps in the river network. In these cases, the choice of polarization could improve the accuracy of the method.

Amitrano et al. (2015) [48] presented a framework for the treatment of multi-temporal Synthetic Aperture Radar (SAR) images that defines an intermediate product between L1 and L2 named L1–α through the fusion between the intensities of the reference and test images and their coherence into a false-color RGB image. The above-mentioned framework was applied to the assessment of morphological variations due to flood events [31]. The au-

thors also verified the possibility of monitoring water bodies: lakes, wetlands, and rivers. For the case of rivers, water channels were automatically extracted by means of an intensity threshold, whereas active channels and sediment bars were visually outlined. Active channel widening and narrowing were highlighted [30].

Obida et al. (2019) [49] applied the K-means unsupervised methodology to cluster Sentinel 1 data for the purpose of extracting the river network of the Niger delta. Subsequently, the centerline of the river network was extracted and compared with manually derived centerlines from imagery acquired in the visible range.

Moharrami et al. [37] employed a simple Otsu algorithm applied to the histogram of an entire Sentinel 1 image to delineate the flooded areas in North Iran for the extreme event of March 2019. In this case, the estimation of the threshold value is particularly challenging, because the target class typically constitutes only a minor portion of the image, and therefore, the histogram does not exhibit a bimodal distribution. One additional aspect is the utilization of a single threshold value for clustering the entire image. Several approaches can be used to address this issue.

In order to parameterize the distribution functions from the histogram of the two classes (dry soil and water), Chini et al. [39] introduced a Hierarchical Split-Based Approach (HSBA) to divide the image into tiles, each with an equal proportion of pixels belonging to the two classes of interest. To achieve this, they checked that the histogram was clearly bimodal, and the parametrization of the distribution function performed well. To cluster the image, they applied a Regional Growing (RG) algorithm. The threshold for the seeds and the tolerance criterion to stop the growing process were selected based on the distribution of the target class estimated by HSBA.

Ciecholewski [35] proposed a two-step global threshold approach for segmenting the river channels. Firstly, the polarimetric ALOS PALSAR image is clustered using a watershed using the immersion algorithm. Secondly, in order to reduce over-segmentation, surrounding sub-regions are iteratively merged by maximizing the average contrast. The algorithm was compared with three other approaches: multilevel image thresholding using Otsu's method (Otsu), Fast Random Walker (FRW), and Active Contour Without Edges (ACWE) on a reach of Sungai Kampar River channel.

Cao et al. [40] proposed subdividing the image into tiles of a fixed dimension $s \times s$ and applying the Bimodality Test (BT) to identify the tiles that exhibit a bimodal histogram. The histograms were smoothed using a Gaussian convolution kernel. The mode value of the water portion of the histogram was utilized as the threshold for identifying the core water area. Lastly, a region-growing algorithm (RGA) was employed to generate a spatially homogeneous water map.

Donchyts et al. [38] introduced an extension of non-parametric detection methods, such as the histogram-based Otsu thresholding algorithm. They incorporated the Canny edge filter to identify the edges between water and dry soil and subsequently computed the histogram using the pixels enclosed within an area surrounding those edges. In this particular case, the histogram obtained displayed a distinct bimodal shape, indicating the suitability of the Otsu thresholding algorithm.

Finally, Tan et al. [41] developed a self-adaptive thresholding algorithm, derived from the Otsu approach, for automatic water extraction using Sentinel-1 Synthetic Aperture Radar (SAR) imagery. This algorithm incorporates the side-looking characteristic of SAR data by subdividing the S1 scene into uniform tiles based on the distance to the orbit. The goodness of the classification was evaluated using the Jeffries–Matusita (JM) distance function. Compared to five other traditional segmentation algorithms (Otsu, Moments, Mean, Isodata, and Minerror), the proposed method achieved the highest overall accuracy.

3. Materials and Methods

This work proposes an unsupervised methodology based on the Google Earth Engine cloud infrastructure for the continuous monitoring of river dynamics during flood events using freely available Sentinel-1 imagery. The proposed method utilizes the Level 1 (L1)—

GRD—product of Synthetic Aperture Radar (SAR) imagery acquired from Sentinel-1 in the Interferometric Wide swath (IW) mode. Sentinel-1 is a C-band active sensor operating at a center frequency of 5.405 GHz, which corresponds to a wavelength of ≈5.5 cm. The sensor returns images at a pixel spacing of 10 m, and the pixel values typically range between −35 decibels (dB) and slightly positive values. IW product is Sentinel-1's primary operational mode over land, and it is available in dual polarization, namely vertically emitted, vertically received (VV) or vertically emitted, horizontally received (VH). The vertical polarization, interacting with the Earth's surface, can return to the satellite sensor in the vertical plane or in the horizontal one. Before ingesting the imagery into the Engine's database, Google applies the required standard preprocessing to the Sentinel-1 Ground Range Detected (GRD) product. This preprocessing involves updating the orbit information, removing image border noise, modeling the thermal noise, calibrating the images radiometrically, and applying terrain correction.

This work proposes the implementation of a processing chain as follows:

- Enriching the image stack with hydrometric data;
- Applying the radiometric slope correction algorithm;
- Reducing speckle noise;
- Extracting the wet channel with a Self-Adaptive Thresholding Approach; and
- Output functions.

Each function was structured in a main body and sub-functions with the purpose of allowing sequential calls needed from the time series of images.

GEE's architecture is based on a client/server programming model. Under this architecture, the client libraries provide a user-friendly programming environment, recording the computational chain and sending it to the server for the execution. This implies that it is impossible to combine Earth Engine library calls (server side) with local processing operations (client side). The procedure has three points where the client site and server side exchange inputs and outputs: the image query step, the upload of hydrometric data, and the output step, which can save scatter plots, time series of water masks, and data dictionaries (Figure 1).

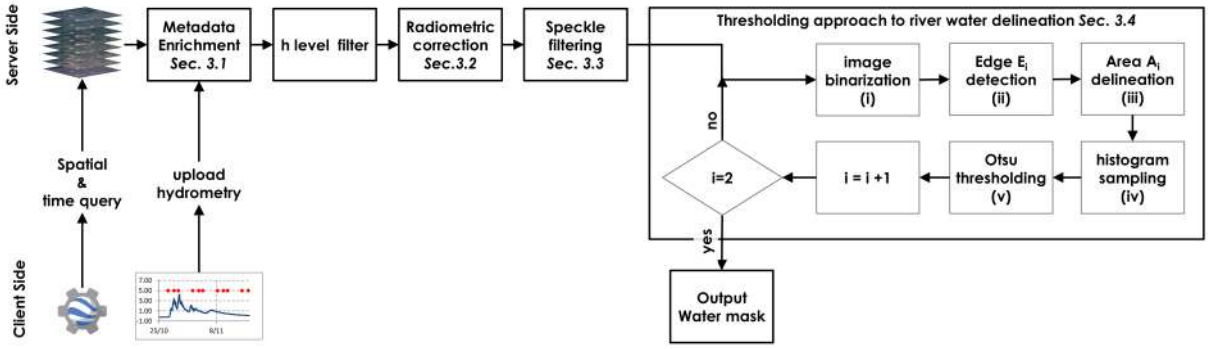

Figure 1. Workflow diagram of the proposed framework for mapping the braided channel area at sub-event time scale using time series of Sentinel-1 imagery (red diamond). The time-varying water level is represented by the blue line.

Previous research has demonstrated that, in scenarios characterized by non-windy conditions and the absence of stream water, VV polarization exhibits superior accuracy to VH polarization [50]. This is attributed to the sensitivity of VV polarization to water surface roughness. VH is generated from the interaction with the tree crowns (volumetric scattering), and part of the backscatter is redirected towards the water channel, causing misclassification [51]. In the case of large gravel bed rivers without vegetation in the active channel, the rippling water surface of the river prevents the exploitation of VV polarization, suggesting the use of the VH one.

3.1. Image Selection and Metadata Enrichment

Images are selected on the basis of a spatial query of the region of interest and a query of the time interval of the flood event. After the initial image query, the metadata of the images are enriched with the hydrometric level registered at the time of image acquisition. This operation is of utmost importance for subsequent analysis as it allows for the determination of inundation dynamics in conjunction with hydrometric levels. This, in turn, facilitates the inference of the relationship between flooded areas and water discharge.

The water-level time series, composed of the date in a string format and the water level in a decimal floating-point format, are firstly converted into a collection of images and then joined with the SAR image collection. The resulting collection contains paired elements composed of the metadata and all the bands of the primary SAR collection and the matching element from the hydrometric level collection. The matching criterion is time-dependent, and SAR images are associated with the nearest water level value according to the following expression:

$$\text{Pixel} = \begin{cases} h_i & if \;\; t_{SAR} \in [t_i; t_{i+1/2}) \\ h_{i+1} & if \;\; t_{SAR} \in [t_{i+1/2}; t_{i+1}] \end{cases} \tag{1}$$

where h_i and h_{i+1} correspond to the water level at time t_i and t_{i+1}, respectively, t_{SAR} is the SAR acquisition time, and $t_{i+1/2} = (t_i + t_{i+1})/2$.

3.2. Radiometric Terrain Correction

Due to the side-looking configuration of SAR sensors, there are a number of geometric and radiometric distortions that arise from the 2D imaging processing of the 3D Earth surfaces and are intrinsically linked to the local orientation of the surface, which need correction and reduction. In the ideal case of a flat surface, the distortion is a specific geometric compression of the ground in the slant range, with increasing distortion moving from the furthest to the nearest range area. The conversion of the slant range to ground range is typically performed by the radar processor prior to image creation. This conversion facilitates accurate distance measurements by accounting for the radar geometry [52].

On the other hand, radiometric distortions caused by terrain orthography need to be corrected using an analytical approach [53–58]. Terrain slopes cause significant variations (radiometric distortions) on radar backscatter values, depending on the angle and aspect of the surface and on the radar configuration, in terms of frequency, polarization, and ascending or descending path. Foreshortening, layover, and shadowing can be included among these effects. The first two happen when the slope is facing towards the sensor, while shadowing occurs on the opposite side of the slope. Foreshortening occurs when the slope in the range direction (α_r) is less than the incidence angle (θ_i), whereas layover appears when the slope exceeds the incidence angle. Shading or shadowing of the opposite side of the slope occurs when the angle $\alpha_r > 90^o - \theta_i$.

In applications related to land monitoring, an accurate backscatter measurement has a central role and allows robust land-cover classification. Therefore, radiometric slope correction is needed in order to reduce these topographic effects on backscattering values and to provide imagery in which pixel values are properly related to the radar backscatter of the scene. In the literature, there are different approaches aiming at reducing radiometric distortion.

In this work, two physical models have been taken into account. These models propose an exact solution for the compensation of slope-induced variations in the backscattered energy. Hoekman [59] considers the effects of forested reliefs on the radar backscatter, as an opaque volume composed of isotropic scatterer elements (Equation (2)), whereas Ulander [54] derives an equation for the radiometric correction, projecting the 3D model of

hillslope without vegetation into the 2D domain of the SAR images and thus considering it as a surface of isotropic scatterers (Equation (3)):

$$\gamma_f^0 = \gamma^0 \cdot \frac{\tan(\pi/2 - \theta_i)}{\tan(\pi/2 - \theta_i + \alpha_r)}, \tag{2}$$

$$\gamma_f^0 = \gamma^0 \cdot \frac{\cos(\alpha_{az}) \cdot \cos(\pi/2 - \theta_i + \alpha_r)}{\cos(\pi/2 - \theta_i + \alpha_r)}, \tag{3}$$

where γ_f^0 and γ^0 are, respectively, the backscatter on a flat terrain and the backscatter on a tilted terrain, α_{az} and α_r are the terrain slope in the azimuth direction and in the range direction. θ_i represents the incidence angle of the SAR signal with the Earth's surface.

3.3. Denoising

The goal of this framework step is to reduce the intrinsic noise of Sentinel 1 SAR images, a granular pattern distribution called speckle that affects the SAR images. This effect is due to the sum of constructive and destructive superpositions of the backscattered signal after the interaction with the target area. In general, the task of all despeckling methods is to reduce the speckle noise without losing fine details and edges of features. Among the approaches used for SAR images despeckling, Bayesian methods [60–64], non-Bayesian algorithms [65–67], hybrid approaches, and also new methodologies based on machine learning algorithms can be mentioned. Comprehensive recent reviews of these methodologies can be found in [68–70].

In this paper, the non-Bayesian model proposed by Perona and Malik (1990) [65] was used, which is based on the Gaussian kernel convolution and maintains an accurate location of feature edges during the process of image smoothing and restoration, through the following definition of a scale space:

$$\begin{cases} I_t = \Delta(c(x, y, t)\nabla I) \\ I_{(t=0)} = I_0 \end{cases} \tag{4}$$

where $I_t = \partial I / \partial t$ is the partial time derivative of the intensity image, I_0 is the initial intensity image, and Δ and ∇ are divergence and gradient operators, respectively. The diffusion coefficient $c(x, y, t)$ is a function of the gradient magnitude of the image. The primary task of the diffusion coefficient is to prioritize smoothing within a region rather than smoothing across its boundaries. This objective can be accomplished by ensuring that the conduction coefficient is a monotonically decreasing function equal to 1 within the interior of each region and 0 at the boundaries. The setting of the diffusion coefficient function is discussed in the next paragraph.

As noticed by [71,72], Gaussian kernel-based methods are equivalent to the solution to the diffusion Equation (Equation (4)), which, neglecting the hierarchy of the image levels, reduce both image noise and the definition of object boundaries. With the aim of overcoming these limitations, Perona, P. & Malik, J. [65] defined the diffusion coefficient as a function of the gradient magnitude of the image $c = g(\|\nabla I\|)$. This function, called the edge stopping function, ensures a higher rate of diffusion within homogeneous regions and avoids the blurring of the feature boundaries characterized by high values of $\|\nabla I\|$.

Three edge stopping functions were tested. The first two (Equations (5) and (6)) were proposed by Perona and Malik [65], and the third (Equation (7)) was proposed by Black et al. [73]:

$$c_1 = e^{-(\|\nabla I\|/K)^2}, \tag{5}$$

$$c_2 = \frac{1}{1 + (\|\nabla I\|/K)^2}, \tag{6}$$

$$c_3 = \begin{cases} \frac{1}{2}\left[1 - \left(\frac{\|\nabla I\|}{K\sqrt{2}}\right)^2\right]^2 : \|\nabla I\| \leq K\sqrt{2} \\ 0 : otherwise, \end{cases} \tag{7}$$

where $\|\nabla I\|$ is the gradient magnitude of the image I, and K is a constant parameter that allows for the adjustment of the noise filter. Its value is typically determined through experimental selection or by considering the noise characteristics present in the image. In the present work, it was set to 3. Figure 2 illustrates the distinct smoothing effects of the three functions mentioned earlier. The c_1 function stops the diffusion starting from a small gradient value, whereas c_2 needs a higher gradient value in order to stop diffusion. The c_3 function stops the diffusion at low gradient values, preserving very fine details. So c_2 privileges wide regions over small ones, c_1 privileges high contrast edges versus lower-contrast edges, and c_3 reduces the diffusion even more rapidly than c_1 and stops diffusion where the gradient is very low.

The most appropriate edge-stopping function in our case is c_1, as it adequately smooths homogeneous regions while preserving border lines.

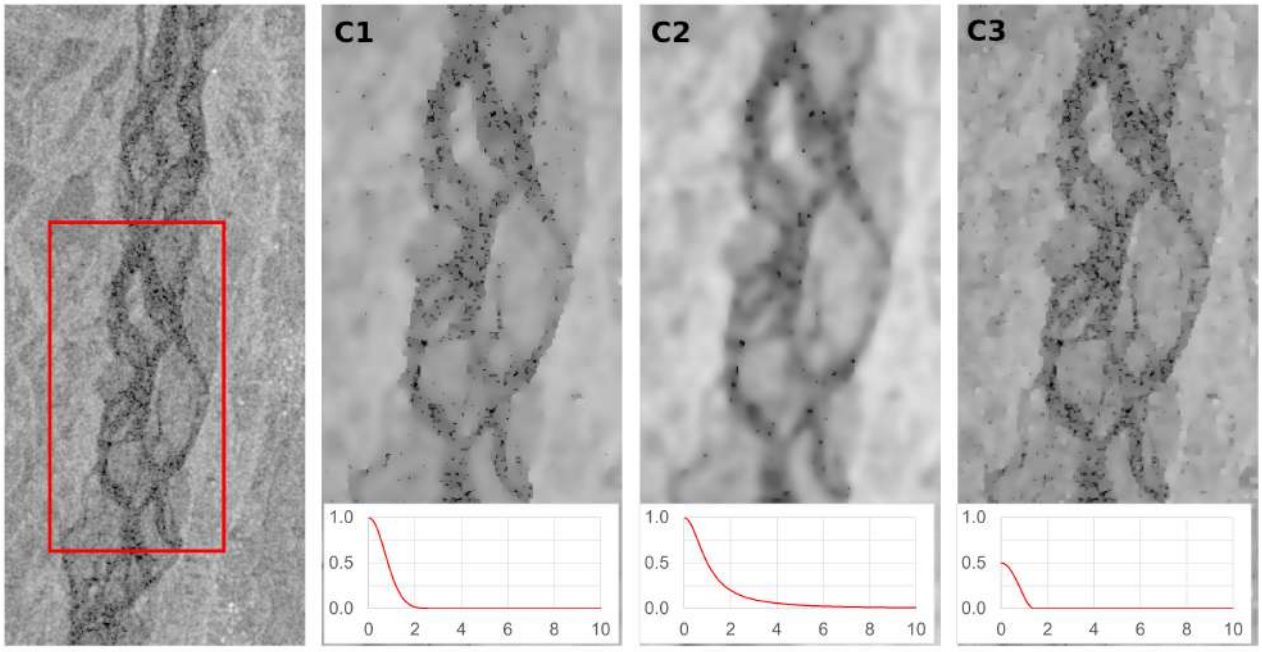

Figure 2. Illustration of the varying smoothing effects of Perona and Malik's model using different edge-stopping functions on Sentinel-1 imagery. From left to right: original VH band, denoised images using Equations (5)–(7). The three denoising functions are plotted in the bottom sub-panels as a function of the gradient magnitude of the image. The *x*-axis represents the gradient magnitude of I $\|\nabla I\|$, while the *y*-axis represents the value of $c_{(\|\nabla I\|)}$.

3.4. Self-Adaptive Thresholding Approach to River Water Delineation

Image segmentation is the process by means of which two or more classes or objects are identified in an image. Various techniques are widely used in research fields such as

medical applications, the recognition and tracking of objects, and environmental analysis, including the delineation of river and waterbodies from optical, multispectral and radar data. Two groups can be mentioned: traditional methods (e.g., edge detection, clustering, random forest, support vector machine, Markov random field, statistical algorithm), and segmentation processes based on the latest Deep Learning (DL) methods (ANN, CNN, and others) [74].

As described in the introduction, in our case, the water class covers only a small portion of the entire scene, leading to a unimodal histogram that represents mainly the dry soil class. Such a histogram makes the Otsu thresholding method almost impossible to use. In order to obtain a bimodal distribution that allows the computation of a reliable threshold value, a suitable subset of the image (A_i) is needed. To this end, the proposed self-adaptive thresholding approach is composed of two cycles ($i = 0, 1$) of the following steps (Figure 1):

(i) Image binarization process using the threshold value t_i;
(ii) Identification of the wet–dry edges E_i using the Canny Edge filter [75];
(iii) Delineation of the area A_i applying a buffer (B_d) around the edges E_i;
(iv) Histogram sampling within the area A_i;
(v) Evaluation of the threshold t_{i+1} applying the Otsu algorithm.

On the first run ($i = 0$), the threshold t_0 is manually set to -20 dB, representing an initial threshold attempt. After the second run ($i = 1$), the algorithm outputs the final threshold t_2, which is then used to extract the water mask. Figure 3 illustrates the conceptual scheme depicting the definition of the edges E_i and the area A_i for the i-th step.

After binarizing the image using t_i (step i of the procedure), the Canny Edge filter is applied to the resulting binary image (step ii of the procedure). Before the edge-detection step, the image is convolved with a Gaussian filter with the parameter σ set to 1. The edges are subsequently defined as those pixels where the magnitude of the gradient exceeds 1.

The area A_i, where the histogram is sampled, is defined by buffering the edges E_i by a distance B_d (step iii of the procedure). The choice of buffer amplitude B_d is bounded by the channel width. At low discharges, the channel width is narrow, whereas it is wider at high discharges. The optimal buffer amplitude is the one that samples half of its area in the channel and the remaining half on dry land, without including other land classes such as vegetation or urban areas with higher backscatter values. In Section 5.1, the impact of the choice of parameters will be presented and analyzed, specifically highlighting that the optimal selection for our specific case is B_d = 50 m.

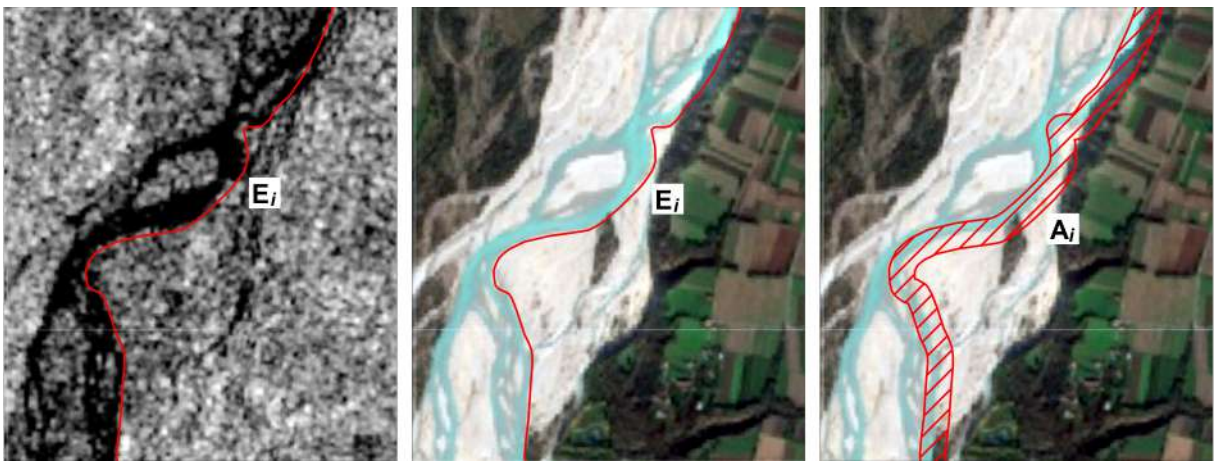

Figure 3. Conceptual scheme of the thresholding algorithm. The first two panels depict the definition of the wet–dry edges, denoted as E_i, based on the threshold t_i. Meanwhile, the right panel illustrates the area A_i generated around these edges with a distance B_d, within which the Otsu algorithm is subsequently applied.

To reduce the computational time and implement an efficient automatic procedure, we selected a thresholding method (step vs. procedure) with low consumption of computational resources, namely the Otsu thresholding algorithm [76], which is simple to implement and has a similar accuracy to more complex methods [77]. The Otsu thresholding algorithm, initially implemented by Donchyts et al. [38], was optimized with the aim of ingesting a stack of images. The algorithm is applied to the decibel (dB) histogram sampled into the area A_i of every SAR image and is based on the maximization of the inter-class variance, defined as

$$\sigma_B^2 = \omega_0 \cdot (\mu_0 - \mu_T)^2 + \omega_1 \cdot (\mu_1 - \mu_T)^2 \tag{8}$$

where σ_B^2 is the inter-class variance, ω_0 and ω_1 are the probabilities of class occurrence, μ_0, μ_1 are the class mean levels, and μ_T is the total mean level.

$$\mu_0 = \sum_{i=1}^{t} \frac{i \cdot p_i}{\omega_0}; \tag{9}$$

$$\mu_1 = \sum_{i=t+1}^{L} \frac{i \cdot p_i}{\omega_1} \tag{10}$$

$$\omega_0 = \sum_{i=1}^{t} p_i; \tag{11}$$

$$\omega_1 = \sum_{i=t+1}^{L} p_i; \tag{12}$$

where L is the number of levels and p_i is defined as the ratio n_i/N. n_i denotes the number of pixels at level i, and N is the total number of pixels.

As mentioned earlier, the successful application of the Otsu algorithm relies on the presence of a distinct bimodal distribution in the histogram. In the scenario where the edge E_i is placed in areas where portions of the image are occupied mainly by water with a small proportion of dry sediments, A_i will be formed mainly by the water class, resulting in a unimodal histogram (Figure 4A). Similarly, if E_i is placed where mainly dry soil is present, A_i will be formed mainly through dry pixels (Figure 4B). In both cases, the Otsu's thresholding algorithm will yield an unreliable threshold. To avoid this, the proposed Self-Adaptive thresholding approach takes advantage of the second run to adjust the position of the wet–dry edges E_i until the sampling area A_i includes approximately 50% of pixels from each class (Figure 4C). In Section 5.1, we will describe the gradual improvement in the bimodality characteristic of the histogram, which is achieved through two cycles of the procedure. Furthermore, we will report the threshold values and the corresponding relative binary masks for the specific case study.

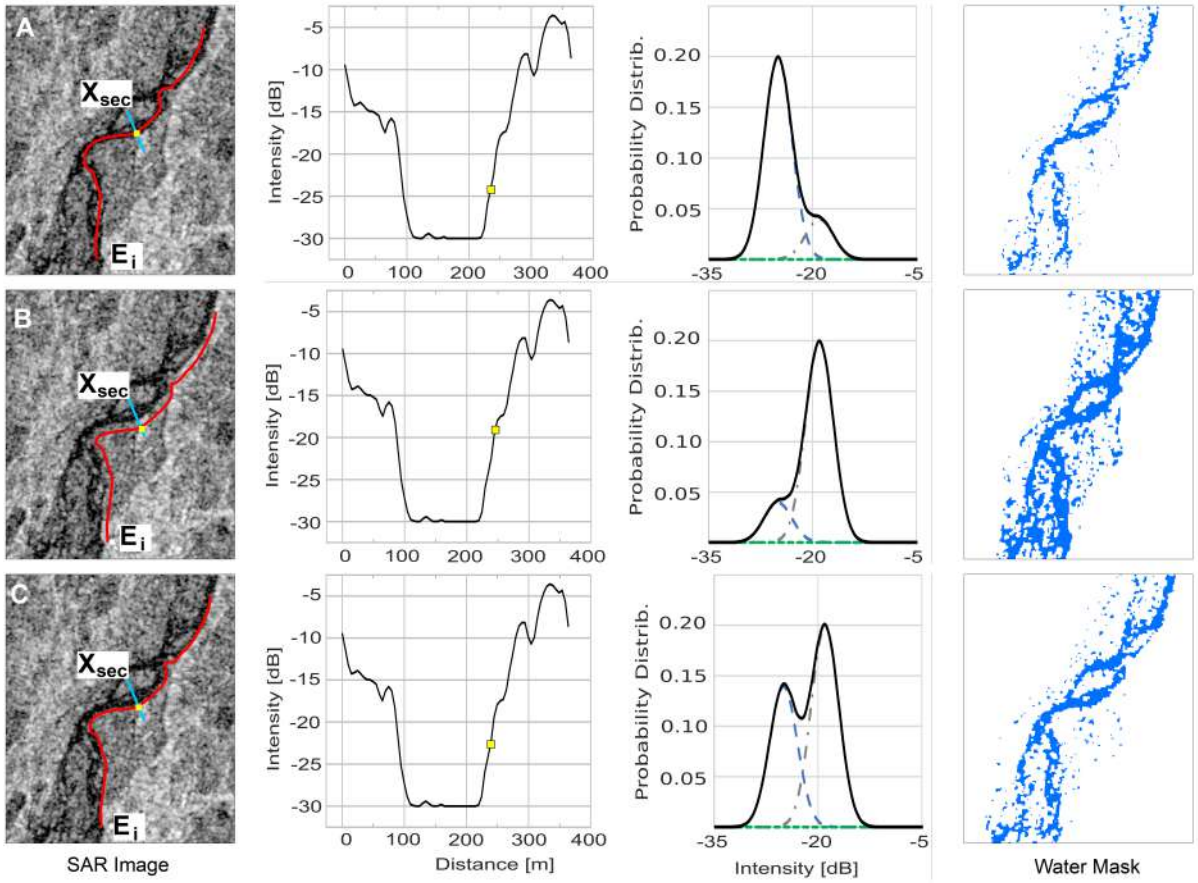

Figure 4. Examples demonstrating the effect of positioning the wet–dry edges E_i on histogram sampling and the resulting water mask. Row (**A**) displays the unimodal histogram generated when the wet–dry edges E_i are positioned in areas of the image predominantly occupied by water, with a small proportion of dry sediments. Conversely, row (**B**) shows the unimodal histogram generated when E_i are placed in areas of the image predominantly occupied by dry sediments. Row (**C**) represents the case when E_i guarantees that the sampling area A_i includes approximately 50% of pixels from each class. The backscatter cross-section highlights the threshold value as a yellow square.

4. Case Study

The proposed algorithm has been applied and tested on the Tagliamento river (north east Italy), a large gravel bed braided river recognized as a reference fluvial system for its near-natural dynamics [78]. Its catchment covers an area of about 2700 km^2 from the Italian Alps to the Adriatic Sea, with a total length of 178 km. The study focuses on a 13 km long reach located in the foothill area of Friulian Pre-Alps, downstream of the Pinzano gorge (Figure 5). It has a mean longitudinal gradient equal to 3.4 m/km and the active channel reaches a width of 1000 m. During flood events, this section of the river shows significant variations in the water surface area, induced by the inundation of lateral channels and sediment bars. The reach is also morphologically active, showing frequent erosion of banks and vegetated islands.

The hydrologic regime of the Tagliamento river can be classified as a pluvio-nival regime [78]. The snow melt during the spring season (April–June) sustains the discharge (Figure 6A), ensuring a period of significant mobility of the riverbed, particularly when associated with rain events. Major floods generally occur in autumn, when heavy rains are more likely, with humid air masses moving north from the sea. In the present work, we used data from the hydrometric station in Venzone, about 20 km upstream of the study reach, with a particular focus on the floods that occurred on October 2018, November 2019, and December 2020 (black arrows in Figure 6B).

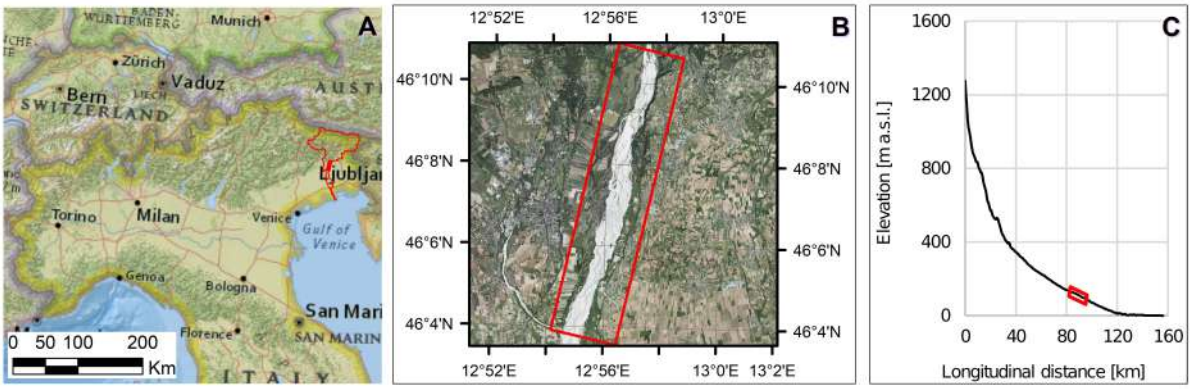

Figure 5. Location of the Tagliamento catchment in north east Italy (frame **A**) and aerial view of the study site (frame **B**). Frame (**C**) displays the longitudinal profile of the river bed, with the red box highlighting the investigated reach.

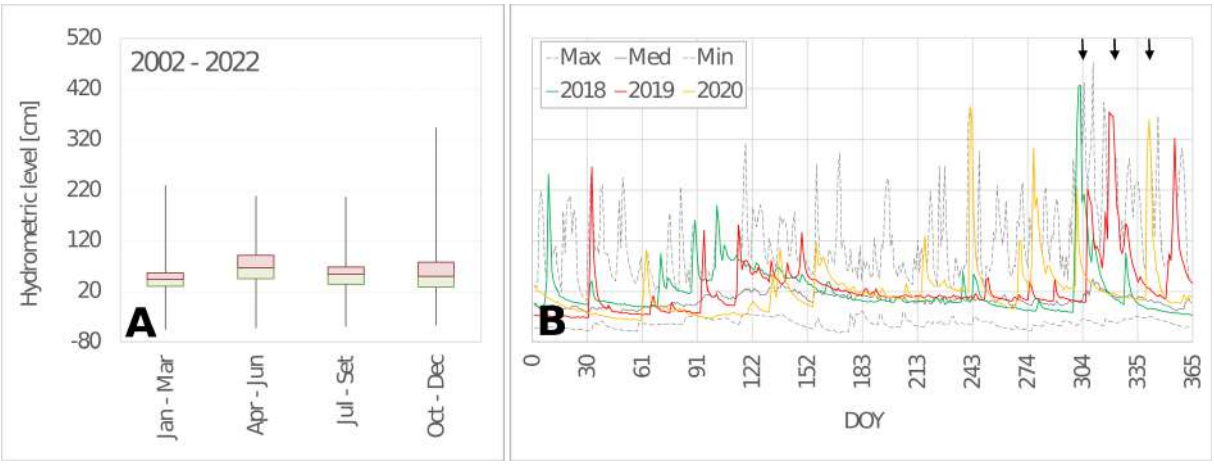

Figure 6. (**A**) seasonal flow variation from 2002 to 2022, and (**B**) flow regime for the years 2018, 2019, and 2020, as measured at the Venzone gouging station. In panel (**B**), the gray solid line and the two gray dashed lines are the median, the maximum, and the minimum value for every single day in the period 2002–2022, respectively.

The new Digital Elevation Model (DEM) of Italy presented by [79] was used to implement the radiometric terrain correction. The DEM was generated through Delaunay tessellation of a heterogeneous dataset, coming from different Italian public bodies. Its vertical accuracy was assessed on an independent set of control points and, in the region of interest, is less than 2 m, which is considered sufficient for the study objectives. The spatial resolution is compatible with the 10 m pixel size of Sentinel-1 imagery.

The correction of the radiometric distortions was performed using the volumetric model (Equation (2)), as suggested by [57,80], for case studies with predominant agricultural land use.

5. Results

In this section, we start by presenting the sensitivity analysis of the thresholding parameters; then, the calibrated procedure is applied to three flood events in October 2018, November 2019, and December 2020, with return intervals of approximately 10, 4 and 3 years, respectively. In particular, we quantified (i) the area inundated by water as a function of the water level and (ii) the lateral bank erosion rate.

5.1. Sensitivity Analysis

Three hundred Sentinel-1 images entirely covering the study reach were analyzed, in the time spans from January 2014 to June 2021. During this period, the hydrometric level at the Venzone gauging station ranged from a low flow up to 4.27 m, which was reached during the flood event named Vaia, which occurred at the end of October 2018. At low flow, particularly during summer, the river bed is often completely dry, due to a natural down-welling process in the huge alluvial sediment deposit [81]. To avoid issues with a completely dry reach, we selected images with a corresponding water level at Venzone larger than 0.25 m.

For each image, the procedure outlined in Section 3 and Figure 1 was applied, obtaining a classified map of the water surface extension and the estimated value of the threshold t_i that better differentiates between water and dry sediments.

The influence of the buffer amplitude B_d on the threshold t_i was investigated through a sensitivity analysis, varying the buffer amplitude from 50 m to 300 m. The 300 values of t_i were then interpolated using a non-parametric kernel distribution with a Gaussian normal distribution function with mean equal to t_i and a bandwidth of 0.25 dB.

Figure 7 shows the effect of increasing the buffer distance from 50 m to 300 m. It is worth pointing out that the active corridor width is about 1000 m, with single channels of the braided network being 50 m to several hundred meters wide. It is therefore reasonable to expect a buffer distance in the proposed range. The comparison between the six probability distribution functions and the fitting curve of the most likely threshold values (Figure 7) shows that, for increasing values of the buffer amplitude, the mode shifts towards positive values. This effect is due to the progressive inclusion of pixels representing other land classes, such as vegetation, characterized by volume backscattering, and thus with a stronger backscatter than water and dry sediments. Most probable values of the threshold t_i range between -19 and -20 dB, with a maximum mode difference of about 1.5 dB. A higher value of the threshold results in more pixels classified as water. Differences are, however, limited, in terms of mapping of the main channels. To keep the procedure simple and automated, our suggestion is to select the lower value of the buffer distance to avoid including a significant number of pixels belonging to other land use classes.

Moreover, the influence of the first value VH_0 was tested for B_d equal to 50 and 100 m, running a second cycle of the thresholding algorithm and imposing the threshold estimate in the first cycle as the initial value. Figure 8 shows the histograms of the pixels included in the area A_h with the estimated threshold t_i represented by the red vertical line. The second run shows a better separation of the two classes, with a clearly bimodal distribution. However, the values of the threshold are only slightly different, resulting in an estimated area of the water surface that differs mainly because of sparse, isolated pixels (red pixels in the right panel in Figure 8). The histograms in the case of B_d equal to 100 m further confirm that, with a wider buffer it is likely the area A_h that includes a third class of land use (vegetation in this case), represented by the third peak at -14 dB that appears clearly on the right of the histograms after the second run.

In summary, the sensitivity analysis indicated that running the algorithm with a buffer width B_d of 50 m yielded favorable results. Additionally, it confirmed the advantages of using a double cycle approach, as it produced histograms with a more distinct bimodal characteristic and reduced the dependence on the initial VH_0 value.

5.2. Inundation Dynamics

The results of the classification of the water surface area for the 300 images from 2014 to 2021 are shown in Figure 9, in terms of the proportion of total active corridor area inundated by water as a function of the hydrometric level at the Venzone gauging station. Hydrometric data were shifted back by 1 h with respect to the image timing, to take into account the flood propagation from Venzone to the study reach. The 1 h shift has been evaluated, referring to a second gauging station and approximated hydraulic computations.

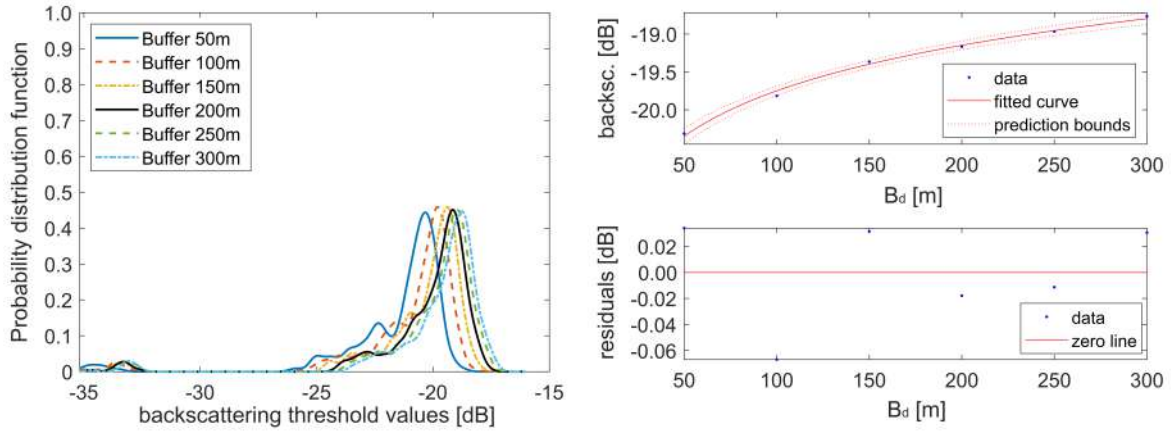

Figure 7. Comparison of the interpolated probability density functions obtained in the six cases, with B_d varying from 50 to 300 m (**left**) and fitting of the most likely threshold values with prediction bounds and residuals (**right**).

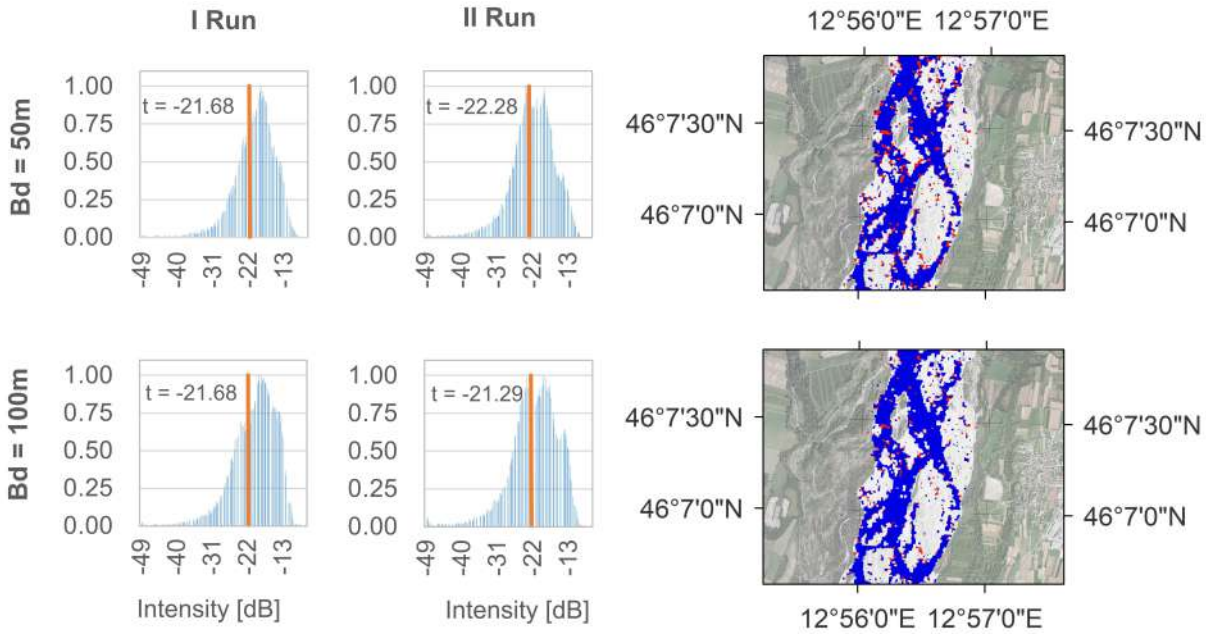

Figure 8. Histograms and the corresponding threshold values obtained after the first and second run of the Otsu thresholding algorithm (first and second column, respectively) in the cases of buffer width B_d set to 50 and 100 m (first and second row, respectively). The panels on the right illustrate the classification differences between the first and second run. The red pixels represent areas that changed from being classified as water after the first run to being classified as dry soil after the second run.

Figure 9 shows two distinct behaviors: (i) for a water level between 0.25 m and 1 m (red points), the proportion of wet areas increases markedly from 20% to 60%; (ii) for a water level higher than 1 m (blue points) the proportion of wet areas increases less rapidly, reaching 100%, i.e., full inundation of the active corridor, for a water level of about 3 m. At flow levels lower than 1 m, the number of channels increases significantly, with the activation of lateral channels and submergence of low bars. For higher water levels, channels start to merge, and the higher bars and vegetated islands are submerged. The values observed from this analysis are similar to what has been observed on shorter reaches by [82,83], who used field surveys and fixed cameras.

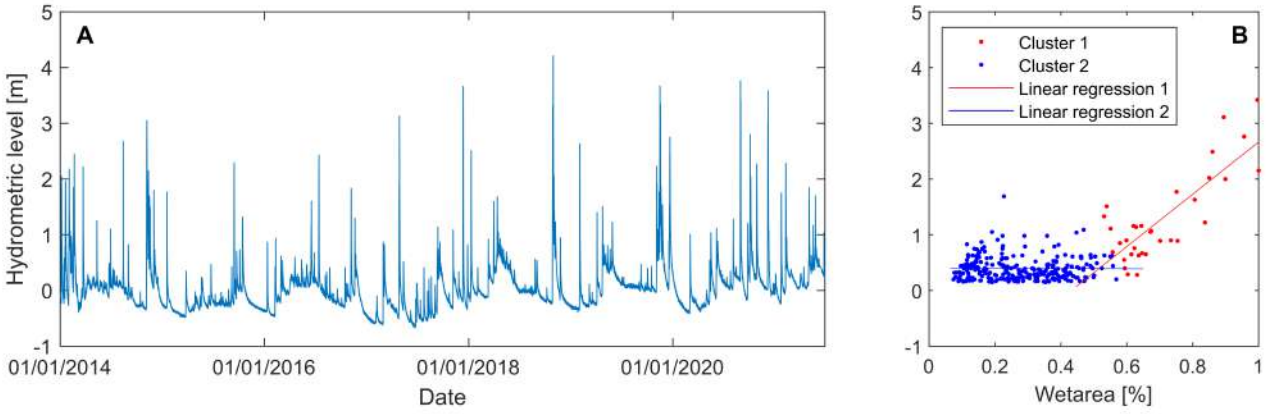

Figure 9. (**A**) Water level recorded at the gauging station of Venzone from 2014 to 2021; (**B**) wet area proportion for the 300 analyzed images.

The potentiality of the SAR images mapping is well expressed by the analysis at the single flood scale, for the events in the October 2018, November 2019, and December 2020 scale (red, yellow, and green arrows in Figure 9A). Figure 10 shows the hydrographs (blue line) registered at the Venzone gauging station and the corresponding time evolution of wet area proportion evaluated at the reach scale (magenta line), for the three events. At the top of each panel, the red points show the acquisition time of the SAR Sentinel-1 images, whereas green points show the available multi-spectral Sentinel-2 images, highlighting the impossibility of evaluating the during-flood dynamics with this passive sensor.

The analysis shows that in all three events, the entire active corridor was inundated (values of the wet area have a proportion up to 1). Moreover, despite the observed changes in the local configuration of the channel network, the analysis shows little variations in the wet area's proportion before and after the flood, indicating a sort of equilibrium at the reach scale. The large variability of the blue points in Figure 9B shows that, particularly at low flow, the channel network configuration may change not only in terms of the location of the channel, but also in terms of the total wet area.

Figure 11 reports with more details the inundation dynamics observed during the event in 2019. November 2019 was a very rainy month, with high flows occurring during the entire month, and five subsequent peaks, with the highest reaching more than 3.5 m. The first five panels show 5 of the 14 classified SAR images for this month, with water level ranging from 0.31 m to 3.29 m. The images help to visualize the increase in the wet area for higher values of the flow level. Moreover, the classified maps show the changes in the channel network before and after the flood, with several channels formed/closed at high flow. The red box in the bottom-left part of the reach highlights a local example of lateral bank erosion. To better observe the morphological changes, a zoomed-in image in the red box is reported in the right panel of Figure 11, with the channel location before the flood mapped in blue and the channel after the flood in red. Bank erosion occurred along 340 m, with an average retreat of about 130 m.

The high temporal resolution of the Sentinel-1 images allows a detailed investigation of the processes of bank erosion. In Figure 12, the time evolution of the cumulative bank erosion (in red) and the erosion velocity (in green) are reported, compared to the flow level (in blue). The analysis shows no erosion during the first three smaller floods, with the bank retreat starting during the major peak. In this phase, the bank was eroded at a rate larger than 1 m/h. The erosion continued for several days, with a rate of tens of cm per hour, even if the flow level decreased to values lower than those of the first three floods. These observations support previous studies, pointing out the role of major floods and bank saturation for the initiation of bank erosion [84].

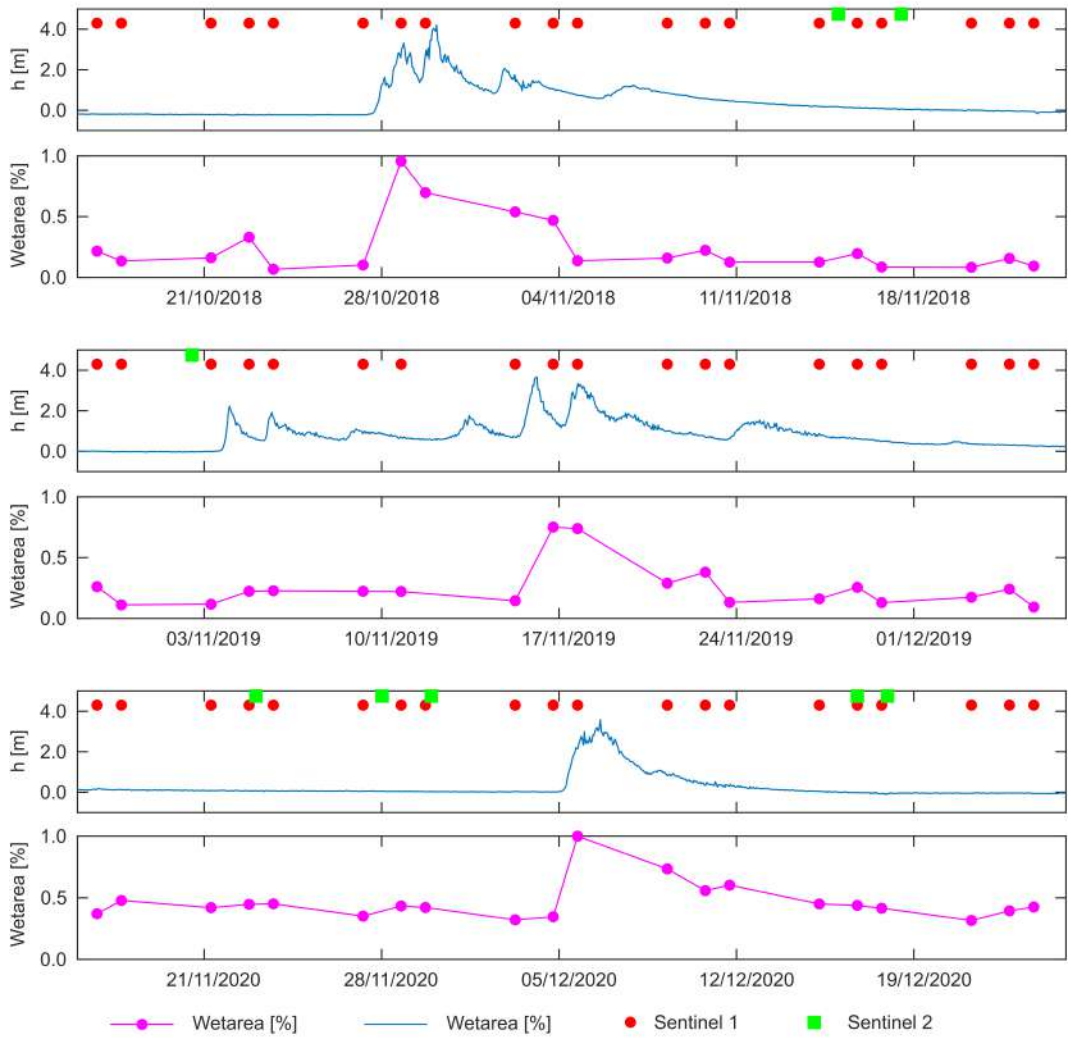

Figure 10. Temporal evolution of water level (blue line) and the corresponding proportion of wet area s (magenta line) for the three floods in October 2018, November 2019, and December 2020 (top to bottom panels, respectively). Red dots are the available Sentinel-1 images and the green dots are the Sentinel-2 available images with cloud cover less than 15%.

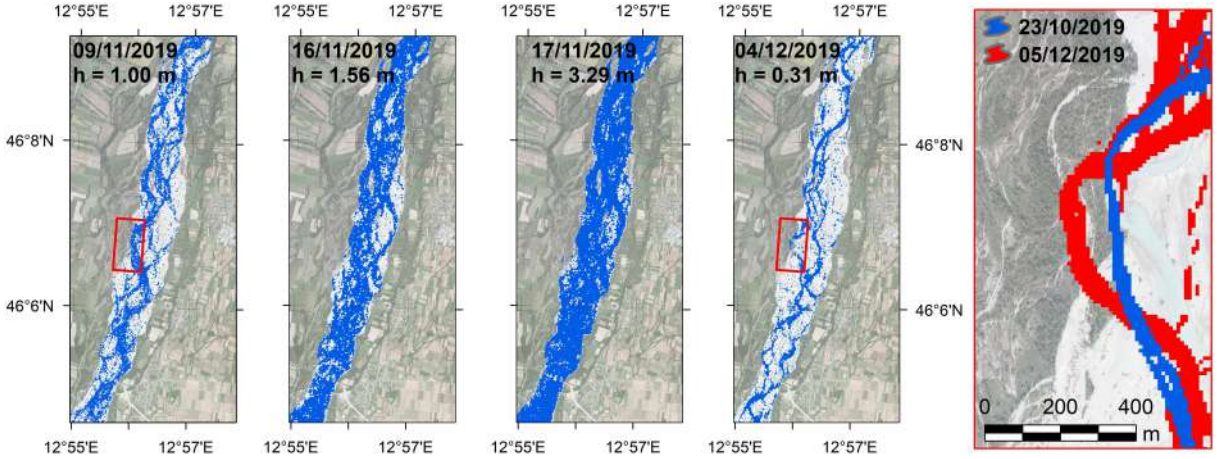

Figure 11. Maps of the estimated wet area during the floods in November 2019, for different values of the water level. The red box locates a major lateral bank erosion event highlighted in the last panel on the right.

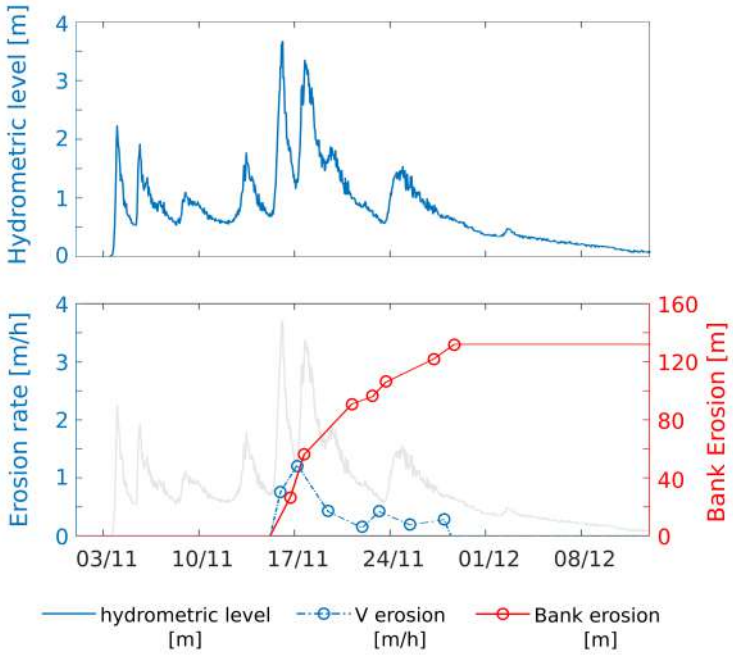

Figure 12. Time evolution of the cumulative lateral erosion (red line) and erosion rate (green line), compared to the flow level measured at the Venzone gauging station (blue line).

6. Discussion and Conclusions

6.1. Potential Implications for Fluvial Geomorphology and River Management

The framework was tested on a 13 km long section of the Tagliamento River, a large and dynamic gravel bed river, where significant changes in the channel network occur frequently. This gave us the opportunity to test the advantages of SAR data to investigate river dynamics at the sub-flood temporal scale. Indeed, SAR imagery is not affected by cloud cover, and this is a foremost advantage when considering flood dynamics. Figure 10 shows the significant difference in usable images considering Sentinel-1 and Sentinel-2 missions, with the latter negatively affected by clouds. Multi-spectral Sentinel-2 imagery provides only before–after flood mapping, rarely allowing for detailed monitoring during floods.

The application was successful in computing the relation between the proportion of the wet area in the active channel and flow level, using 300 images over a period of 7 years. Similar analysis on close-by reaches made in the past [82,83] involved time-consuming field measurements and the installation of fixed cameras to overcome the lack of remotely sensed imagery at a high flow. The possibility of easily extending this application to other reaches on the same river and in other catchments opens up new perspectives for river managers, as it provides the opportunity to assess changes caused by human intervention or by natural processes, in both the inundation dynamics and temporal evolution of the morphology.

From a management perspective, the proposed method has a twofold relevance for both environmental protection and hydraulic risk mitigation. Indeed, the relationship between the time-varying wet area and the river flood stage can be considered as a proxy for assessing the availability and temporal dynamics of aquatic habitats in the target reach. This is particularly relevant in braided or multi-thread rivers, where habitat evaluation with standard, field-based methods still poses relevant challenges [85]. Information made available through the proposed method can support decision-making processes associated with ecological flow design because it readily quantifies the maximum possible spatial extent of aquatic available habitat under a broad set of flow conditions. Furthermore, its capability of providing information with high temporal resolution on channel inundation during floods greatly facilitates the assessment of inundation risk areas, which is at the basis of prevention measures for mitigating flood risk. In the global context of increasing anthropogenic stressors on river systems at multiple scales [86], as well as the rising impact

of climate stressors that can influence flood frequency, duration, and intensity, the proposed algorithm can be critical in disentangling those relations. It is particularly valuable during periods when other remote sensing sources may be limited, especially during flood events.

Furthermore, the proposed mapping procedure proved valid in quantifying river bank erosion rates at the scale of single floods. Bank erosion is a relevant morphological process that affects river evolution and ecology [87]. Predicting and modeling river bank erosion is a challenging task because it strongly depends on local effects as well as a combination of hydraulic and geotechnical processes of the river and the bank itself, including the root reinforcement in the presence of riparian vegetation. To improve our ability to model this process, more observations and quantitative data are essential. Recently, [88] proposed a global inventory of riverbank erosion, based on Landsat imagery of the last 20 years, confirming channel width as the main control but also highlighting large variability among rivers. Our application showed that SAR data can be successfully used to quantify riverbank erosion at the event scale, producing valuable information on the erosion rate at a daily scale, compared to the monthly/yearly scale of previous remote sensing applications. This allowed for an accurate evaluation of when the bank erosion process started, as well as the relationship with the flow level and its variations in time. Similarly to what has been discussed for the mapping of wet areas, the proposed procedure has the potential to detect bank erosion events at a much finer temporal scale, providing highly valuable data for river management but also for the calibration and validation of morphological numerical models. These observations can help with understanding the response of rivers with complex morphology to climate and anthropogenic stressors, quantifying the lateral shift of channels and their morphological dynamics.

This algorithm is focused on the analysis at the flood-event time scale, while the river management shall also consider longer-term effects. It is known that the river morphology can be heavily modified because of anthropogenic stressors and also due to climate variability. Despite the possibility of extracting multi annual time-series of the wet area also covering flood events for the same reach, the application of our algorithm can also provide relevant information at those longer time scales.

6.2. Advantages, Limitations, and Further Development of the Proposed Procedure

This paper presented an unsupervised and cloud-based algorithm, developed within the Python API of Google Earth Engine, that allows the processing of a Sentinel-1 image stack for the automatic detection of river flood dynamics and the associated morphological evolution. As recently pointed out by [89], GEE is a computing platform that can help geomorphologists (and other scientists) using huge amounts of spatially and temporally rich data (in the order of petabytes), overcoming the limitations caused by computing and data storage costs. Remote sensing data significantly transformed fluvial geomorphology in the last decade [14], with most applications involving multi-spectral passive aerial or satellite imagery [90]. Active SAR satellite data such as Sentinel-1 imagery have been demonstrated to provide a valuable asset to map inundated areas [49,91,92], with high accuracy of the water mapping when compared to other sources.

Our investigation confirms the potential of this technique and shows that an unsupervised, cloud-based algorithm produces accurate results, with limited need for parameter calibration. In particular, the analysis pointed out the effect of the buffer distance from the estimated edges B_d and of the starting value of the backscattering threshold VH_0 needed to compute the initial wet–dry edges. We showed that a relatively small buffer width (compared to the channel width) seems more appropriate to avoid including other land classes in the area of interest where the histograms will be produced. Furthermore, through the sensitivity analysis, we demonstrated that, with a second cycle of the Otsu function [76], and with the first computed threshold as starting point for the second run, we can increase the accuracy of the model, making the threshold value independent of the initial attempt value VH_0 and producing a more clearly bimodal histogram. In this way, the selected Otsu thresholding algorithm is most efficient. However, differences are not

large, and a cost/benefit analysis depends on the objectives of the study. Our approach extends the method proposed by Donchyts et al. [38] and differs from those presented by Chini et al. [39], Cao et al. [40], and Tan et al. [41]. Indeed, after the tiling process of the images, their methods need to identify the tiles that are more suitable for evaluating the threshold. This was achieved by applying methods such as the Jeffries–Matusita (JM) distance function [93], the Bimodality Test (BT) [94], and the KMM algorithm proposed by Ashman [95]. The self-adaptive Otsu algorithm proposed in this paper adjusts the sampling area in such a way that the number of wet pixels is approximately equal to the number of dry pixels. Therefore, the method does not require a bimodality check of the histogram.

Moreover, the proposed procedure is designed to enrich the imagery metadata through flow levels at the time of image acquisition. Wherever such flow data are available, the GEE procedure automatically extracts images above, below, or in between the defined thresholds, allowing for correlations to be established between the wet area and flow rate and last but not least significantly reducing the computation time and the operator intervention. This approach can be also applied to other fields of research. Integrating data coming from the near-daily monitoring of river surface temperature (RST) using satellite-based observations could provide valuable support for analyzing the impact of climate change on rivers [96], the study of the interaction between hydro-thermopeaking downstream the hydropower plants and summer heatwaves [97], and the improvement in the quality monitoring of river water [98].

As described in Section 3.3, the value of K was set manually at a fixed value. However, an alternative approach suggests choosing K based on the estimation of the noise level present in the image. As highlighted by Singh et al. [69], the distribution that best represents the statistical distribution of speckle noise in SAR images is a generalized Gamma probability distribution [99,100]. We propose modifying the fixed-value approach by considering K as a function of the variance of the generalized Gamma distribution function.

The planimetric output for the flooded areas exhibits jaggedness as a result of speckling in SAR data caused by both existing vegetation and water motion, which creates a rippling effect on the water surface. Despite the application of denoising operations, the inherent variability of the backscatter signal has made it challenging to achieve continuous classification, thereby posing a challenge for future development of the methodology. The uncertainty in SAR-based flood mapping related to the speckle phenomenon has been addressed in many studies [101,102]. The methodologies that address this issue range from denoising approaches in the preprocessing phase to complex and computationally intensive clustering techniques. Taking inspiration from these studies and ensuring that performance will not be compromised, we intend to reduce fragmentation by incorporating an additional step of regional growing (RG) into the proposed approach [103].

Furthermore, another element of uncertainty in the delineation of flooded areas is related to the presence in silico of nearby dense canopy cover that induces a higher frequency of misclassification. This is due to the interaction of the C-band SAR signal with the treetops, which prevents the signal from reaching the water's surface [104]. A potential advancement in the proposed processing chain could involve the integration of C-band and L-band SAR sensors, as suggested by Pierdicca et al. [105]. This coupling of different SAR wavelengths has the potential to enhance the accuracy and robustness of the flood area delineation process.

Another element that influences the accuracy and robustness of the water surface delineation, while also reducing planimetric fragmentation of the braided river network, is the ground resolution of the SAR data. Sentinel-1 images, with a ground resolution of 5 m $\times$ 20 m and pixel spacing of 10 m $\times$ 10 m, limit the application to rivers larger than a few hundred meters, thereby excluding channels smaller than pixel size. Higher ground-resolution satellites already exist (e.g., COSMO SkyMed and ICEYE) although they are not easily available as Sentinel-1. However, the fast-evolving number and technological capabilities of satellites will soon provide freely accessible imagery at meter or sub-meter

resolution, opening the possibility of integrating multi-mission data and achieving sub-daily monitoring of river dynamics during flood events.

Currently, the processing chain is implemented for the VH band of Sentinel-1 data. With the aim of enhancing the accuracy and robustness of the flood-area-delineation process, we intend to further couple the two bands VH and VV in the processing chain.

The current process requires minimal computational effort, enabling the analysis of 15–20 images of a flood event within a few minutes.

Author Contributions: Conceptualization: A.V., W.B. and G.Z. Data curation: D.R. Formal analysis: D.R. and A.V. Methodology: D.R., A.V. and W.B. Software: D.R. Supervision: A.V., W.B. and G.Z. Writing—original draft: D.R. Writing—review & editing. A.V., W.B. and G.Z. All authors have read and agreed to the published version of the manuscript.

Funding: The authors acknowledge the Italian Ministry of Education, Universities and Research (MUR) in the framework of the project DICAM-EXC (Departments of Excellence 2023–2027, grant L232/2016).

Data Availability Statement: The The Level 1 (L1) GRD product of Synthetic Aperture Radar (SAR) imagery acquired from Sentinel-1 and associated metadata are available at the Earth Engine's public data archive: https://developers.google.com/earth-engine/datasets/catalog/COPERNICUS_S1_GRD (accessed on 1 January 2022).

Conflicts of Interest: The authors declare no conflict of interest.

References

1. Anderson, E.P.; Jackson, S.; Tharme, R.E.; Douglas, M.; Flotemersch, J.E.; Zwarteveen, M.; Lokgariwar, C.; Montoya, M.; Wali, A.; Tipa, G.T.; et al. Understanding rivers and their social relations: A critical step to advance environmental water management. *WIREs Water* **2019**, *6*, e1381. [CrossRef] [PubMed]
2. Petsch, D.K.; Cionek, V.d.M.; Thomaz, S.M.; dos Santos, N.C.L. Ecosystem services provided by river-floodplain ecosystems. *Hydrobiologia* **2022**, *850*, 2563–2584. [CrossRef]
3. Tockner, K.; Stanford, J.A. Riverine flood plains: Present state and future trends. *Environ. Conserv.* **2002**, *29*, 308–330. [CrossRef]
4. Fryiers, K.A.; Brierley, G.J. Geomorphic Analysis of River Systems. In *Geomorphic Analysis of River Systems: An Approach to Reading the Landscape*; John Wiley and Sons, Ltd.: Hoboken, NJ, USA, 2012; pp. 1–345. [CrossRef]
5. Corenblit, D.; Tabacchi, E.; Steiger, J.; Gurnell, A.M. Reciprocal interactions and adjustments between fluvial landforms and vegetation dynamics in river corridors: A review of complementary approaches. *Earth-Sci. Rev.* **2007**, *84*, 56–86. [CrossRef]
6. Sarker, S.; Sarker, T.; Leta, O.T.; Raihan, S.U.; Khan, I.; Ahmed, N. Understanding the Planform Complexity and Morphodynamic Properties of Brahmaputra River in Bangladesh: Protection and Exploitation of Riparian Areas. *Water* **2023**, *15*, 1384. [CrossRef]
7. Phillips, J.D. Evolutionary geomorphology: Thresholds and nonlinearity in landform response to environmental change. *Hydrol. Earth Syst. Sci.* **2006**, *10*, 731–742. [CrossRef]
8. Fryirs, K.A. River sensitivity: A lost foundation concept in fluvial geomorphology. *Earth Surf. Process. Landf.* **2017**, *42*, 55–70. [CrossRef]
9. European Commission. Water Framework Directive, 2000. Available online: https://eur-lex.europa.eu/eli/dir/2000/60/oj (accessed on 1 January 2022).
10. European Commission. Flood Directive, 2007. Available online: https://eur-lex.europa.eu/eli/dir/2007/60/oj (accessed on 1 January 2022).
11. Tariq, M.A.U.R.; Farooq, R.; van de Giesen, N. A Critical Review of Flood Risk Management and the Selection of Suitable Measures. *Appl. Sci.* **2020**, *10*, 8752. [CrossRef]
12. Powers, J.; Klemp, J.; Skamarock, W.; Davis, C.; Dudhia, J.; Gill, D.; Coen, J.; Gochis, D.; Ahmadov, R.; Peckham, S.; et al. The Weather Research and Forecasting (WRF) Model: Overview, System Efforts, and Future Directions. *Bull. Am. Meteorol. Soc.* **2017**, *98*, 1717–1737. [CrossRef]
13. Giannaros, C.; Dafis, S.; Stefanidis, S.; Giannaros, T.; Koletsis, I.; Oikonomou, C. Hydrometeorological analysis of a flash flood event in an ungauged Mediterranean watershed under an operational forecasting and monitoring context. *Meteorol. Appl.* **2022**, *29*, e2079. [CrossRef]
14. Piégay, H.; Arnaud, F.; Belletti, B.; Bertrand, M.; Bizzi, S.; Carbonneau, P.; Dufour, S.; Liébault, F.; Ruiz-Villanueva, V.; Slater, L. Remotely sensed rivers in the Anthropocene: State of the art and prospects. *Earth Surf. Process. Landf.* **2020**, *45*, 157–188. [CrossRef]
15. Reichstein, M.; Camps-Valls, G.; Stevens, B.; Jung, M.; Denzler, J.; Carvalhais, N.; Prabhat, F. Deep learning and process understanding for data-driven Earth system science. *Nature* **2019**, *566*, 195–204. [CrossRef] [PubMed]

16. Gomes, V.C.F.; Queiroz, G.R.; Ferreira, K.R. An Overview of Platforms for Big Earth Observation Data Management and Analysis. *Remote Sens.* **2020**, *12*, 1253. [CrossRef]
17. Smith, L. Satellite remote sensing of river inundation area, stage, and discharge: A review. *Hydrol. Process.* **1997**, *11*, 1427–1439. [CrossRef]
18. Pavelsky, T.M.; Smith, L.C. RivWidth: A Software Tool for the Calculation of River Widths From Remotely Sensed Imagery. *IEEE Geosci. Remote Sens. Lett.* **2008**, *5*, 70–73. [CrossRef]
19. Monegaglia, F.; Zolezzi, G.; Güneralp, I.; Henshaw, A.J.; Tubino, M. Automated extraction of meandering river morphodynamics from multitemporal remotely sensed data. *Environ. Model. Softw.* **2018**, *105*, 171–186. [CrossRef]
20. Pekel, J.F.; Cottam, A.; Gorelick, N.; Belward, A.S. High-resolution mapping of global surface water and its long-term changes. *Nature* **2016**, *540*, 418–4220. [CrossRef]
21. Isikdogan, F.; Bovik, A.; Passalacqua, P. RivaMap: An automated river analysis and mapping engine. *Remote Sens. Environ.* **2017**, *202*, 88–97. [CrossRef]
22. Spada, D.; Molinari, P.; Bertoldi, W.; Vitti, A.; Zolezzi, G. Multi-Temporal Image Analysis for Fluvial Morphological Characterization with Application to Albanian Rivers. *ISPRS Int. J. Geo-Inf.* **2018**, *7*, 314. [CrossRef]
23. Brakenridge, G.R.; Knox, J.C.; Paylor, E.D.; Magilligan, F.J. Radar remote sensing aids study of the Great Flood of 1993. *Eos Trans. Am. Geophys. Union* **1994**, *75*, 521–527. [CrossRef]
24. Smith, L.; Isacks, B.; Forster, R.; Bloom, A.; Preuss, I. Estimation of Discharge From Braided Glacial Rivers Using ERS 1 Synthetic Aperture Radar: First Results. *Water Resour. Res.* **1995**, *31*, 1325–1329. [CrossRef]
25. Nykanen, D.; Foufoula-Georgiou, E.; Sapozhnikov, V. Study of spatial scaling in braided river patterns using synthetic aperture radar imagery. *Water Resour. Res.* **1998**, *34*, 1795–1808. [CrossRef]
26. Dellepiane, S.; Angiati, E.; Vernazza, G. Processing and segmentation of COSMO-SkyMed images for flood monitoring. In Proceedings of the 2010 IEEE International Geoscience and Remote Sensing Symposium, Honolulu, HI, USA, 25–30 July 2010; pp. 4807–4810. [CrossRef]
27. Pulvirenti, L.; Chini, M.; Pierdicca, N.; Guerriero, L.; Ferrazzoli, P. Flood monitoring using multi-temporal COSMO-SkyMed data: Image segmentation and signature interpretation. *Remote Sens. Environ.* **2011**, *115*, 990–1002. [CrossRef]
28. Amitrano, D.; Di Martino, G.; Iodice, A.; Riccio, D.; Ruello, G. An end-user-oriented framework for the classification of multitemporal SAR images. *Int. J. Remote Sens.* **2016**, *37*, 248–261. [CrossRef]
29. Amitrano, D.; Di Martino, G.; Iodice, A.; Riccio, D.; Ruello, G. Unsupervised Rapid Flood Mapping Using Sentinel-1 GRD SAR Images. *IEEE Trans. Geosci. Remote Sens.* **2018**, *56*, 3290–3299. [CrossRef]
30. Papa, M.N.; Ruello, G.; Mitidieri, F.; Amitrano, D. Advanced Technologies for Satellite Monitoring of Water Resources. In Proceedings of the Frontiers in Water-Energy-Nexus—Nature-Based Solutions, Advanced Technologies and Best Practices for Environmental Sustainability, Salerno, Italy, 14–17 November 2018; Naddeo, V., Balakrishnan, M., Choo, K.H., Eds.; Springer International Publishing: Cham, Switzerland, 2020; pp. 157–160. [CrossRef]
31. Mitidieri, F.; Papa, M.N.; Amitrano, D.; Ruello, G. River morphology monitoring using multitemporal SAR data: Preliminary results. *Eur. J. Remote Sens.* **2016**, *49*, 889–898. [CrossRef]
32. Pulvirenti, L.; Marzano, F.S.; Pierdicca, N.; Mori, S.; Chini, M. Discrimination of Water Surfaces, Heavy Rainfall, and Wet Snow Using COSMO-SkyMed Observations of Severe Weather Events. *IEEE Trans. Geosci. Remote Sens.* **2014**, *52*, 858–869. [CrossRef]
33. Pulvirenti, L.; Pierdicca, N.; Chini, M.; Guerriero, L. Monitoring Flood Evolution in Vegetated Areas Using COSMO-SkyMed Data: The Tuscany 2009 Case Study. *IEEE J. Sel. Top. Appl. Earth Obs. Remote Sens.* **2013**, *6*, 1807–1816. [CrossRef]
34. Klemenjak, S.; Waske, B.; Valero, S.; Chanussot, J. Automatic Detection of Rivers in High-Resolution SAR Data. *IEEE J. Sel. Top. Appl. Earth Obs. Remote Sens.* **2012**, *5*, 1364–1372. [CrossRef]
35. Ciecholewski, M. River channel segmentation in polarimetric SAR images: Watershed transform combined with average contrast maximisation. *Expert Syst. Appl.* **2017**, *82*, 196–215. [CrossRef]
36. Zhou, S.; Kan, P.; Silbernagel, J.; Jin, J. Application of Image Segmentation in Surface Water Extraction of Freshwater Lakes using Radar Data. *ISPRS Int. J. Geo-Inf.* **2020**, *9*, 424. [CrossRef]
37. Moharrami, M.; Javanbakht, M.H.; Attarchi, S. Automatic flood detection using sentinel-1 images on the google earth engine. *Environ. Monit. Assess.* **2021**, *193*, 248. [CrossRef] [PubMed]
38. Donchyts, G.; Schellekens, J.; Winsemius, H.; Eisemann, E.; Van de Giesen, N. A 30 m Resolution Surface Water Mask Including Estimation of Positional and Thematic Differences Using Landsat 8, SRTM and OpenStreetMap: A Case Study in the Murray-Darling Basin, Australia. *Remote Sens.* **2016**, *8*, 386. [CrossRef]
39. Chini, M.; Hostache, R.; Giustarini, L.; Matgen, P. A Hierarchical Split-Based Approach for Parametric Thresholding of SAR Images: Flood Inundation as a Test Case. *IEEE Trans. Geosci. Remote Sens.* **2017**, *55*, 6975–6988. [CrossRef]
40. Cao, H.; Zhang, H.; Wang, C.; Zhang, B. Operational Flood Detection Using Sentinel-1 SAR Data over Large Areas. *Water* **2019**, *11*, 786. [CrossRef]
41. Tan, J.; Tang, Y.; Liu, B.; Zhao, G.; Mu, Y.; Sun, M.; Wang, B. A Self-Adaptive Thresholding Approach for Automatic Water Extraction Using Sentinel-1 SAR Imagery Based on OTSU Algorithm and Distance Block. *Remote Sens.* **2023**, *15*, 2690. [CrossRef]
42. Pai, M.M.; Mehrotra, V.; Aiyar, S.; Verma, U.; Pai, R.M. Automatic Segmentation of River and Land in SAR Images: A Deep Learning Approach. In Proceedings of the 2019 IEEE Second International Conference on Artificial Intelligence and Knowledge Engineering (AIKE), Sardinia, Italy, 3–5 June 2019; pp. 15–20. [CrossRef]

43. Pai, M.; Mehrotra, V.; Verma, U.; Pai, R. Improved Semantic Segmentation of Water Bodies and Land in SAR Images Using Generative Adversarial Networks. *Int. J. Semant. Comput.* **2020**, *14*, 55–69. [CrossRef]
44. Chen, L.; Zhang, P.; Xing, J.; Li, Z.; Xing, X.; Yuan, Z. A Multi-Scale Deep Neural Network for Water Detection from SAR Images in the Mountainous Areas. *Remote Sens.* **2020**, *12*, 3205. [CrossRef]
45. Zhang, J.; Xing, M.; Sun, G.C.; Chen, J.; Li, M.; Hu, Y.; Bao, Z. Water Body Detection in High-Resolution SAR Images With Cascaded Fully-Convolutional Network and Variable Focal Loss. *IEEE Trans. Geosci. Remote Sens.* **2021**, *59*, 316–332. [CrossRef]
46. Verma, U.; Chauhan, A.; Manohara, M.P.; Pai, R. DeepRivWidth: Deep learning based semantic segmentation approach for river identification and width measurement in SAR images of Coastal Karnataka. *Comput. Geosci.* **2021**, *154*, 104805. [CrossRef]
47. Yuan, D.; Wang, C.; Wu, L.; Yang, X.; Guo, Z.; Dang, X.; Zhao, J.; Li, N. Water Stream Extraction via Feature-Fused Encoder-Decoder Network Based on SAR Images. *Remote Sens.* **2023**, *15*, 1559. [CrossRef]
48. Amitrano, D.; Di Martino, G.; Iodice, A.; Riccio, D.; Ruello, G. A New Framework for SAR Multitemporal Data RGB Representation: Rationale and Products. *IEEE Trans. Geosci. Remote Sens.* **2015**, *53*, 117–133. [CrossRef]
49. Obida, C.B.; Blackburn, G.A.; Whyatt, J.D.; Semple, K.T. River network delineation from Sentinel-1 SAR data. *Int. J. Appl. Earth Obs. Geoinf.* **2019**, *83*, 101910. [CrossRef]
50. Twele, A.; Cao, W.; Plank, S.; Martinis, S. Sentinel-1-based flood mapping: A fully automated processing chain. *Int. J. Remote Sens.* **2016**, *37*, 2990–3004. [CrossRef]
51. Jong-Sen Lee, E.P. (Ed.) *Polarimetric Radar Imaging*; CRC Press: Boca Raton, FL, USA, 2009. [CrossRef]
52. Freeman, A. SAR calibration: An overview. *IEEE Trans. Geosci. Remote Sens.* **1992**, *30*, 1107–1121. [CrossRef]
53. van Zyl, J.; Chapman, B.; Dubois, P.; Shi, J. The effect of topography on SAR calibration. *IEEE Trans. Geosci. Remote Sens.* **1993**, *31*, 1036–1043. [CrossRef]
54. Ulander, L.M.H. Radiometric slope correction of synthetic-aperture radar images. *IEEE Trans. Geosci. Remote Sens.* **1996**, *34*, 1115–1122. [CrossRef]
55. Luckman, A. Correction of SAR imagery for variation in pixel scattering area caused by topography. *IEEE Trans. Geosci. Remote Sens.* **1998**, *36*, 344–350. [CrossRef]
56. Lee, J.S.; Schuler, D.; Ainsworth, T. Polarimetric SAR data compensation for terrain azimuth slope variation. *IEEE Trans. Geosci. Remote Sens.* **2000**, *38*, 2153–2163. [CrossRef]
57. Hoekman, D.; Reiche, J. Multi-model radiometric slope correction of SAR images of complex terrain using a two-stage semi-empirical approach. *Remote Sens. Environ.* **2015**, *156*, 1–10. [CrossRef]
58. Imperatore, P.; Di Martino, G. SAR Radiometric Calibration Based on Differential Geometry: From Theory to Experimentation on SAOCOM Imagery. *Remote Sens.* **2023**, *15*, 1286. [CrossRef]
59. Hoekman, D.H. *Radar Remote Sensing Data for Applications in Forestry*; Wageningen University and Research: Wageningen, The Netherlands, 1990.
60. Lee, J.S. Digital Image Enhancement and Noise Filtering by Use of Local Statistics. *IEEE Trans. Pattern Anal. Mach. Intell.* **1980**, *PAMI-2*, 165–168. [CrossRef] [PubMed]
61. Lee, J.S. Refined filtering of image noise using local statistics. *Comput. Graph. Image Process.* **1981**, *15*, 380–389. [CrossRef]
62. Frost, V.S.; Stiles, J.A.; Shanmugan, K.S.; Holtzman, J.C. A Model for Radar Images and Its Application to Adaptive Digital Filtering of Multiplicative Noise. *IEEE Trans. Pattern Anal. Mach. Intell.* **1982**, *PAMI-4*, 157–166. [CrossRef]
63. Lopes, A.; Nezry, E.; Touzi, R.; Laur, H. Maximum A Posteriori Speckle Filtering Furthermore, First Order Texture Models In Sar Images. In Proceedings of the 10th Annual International Symposium on Geoscience and Remote Sensing, College Park, MD, USA, 20–24 May 1990; pp. 2409–2412. [CrossRef]
64. Baraldi, A.; Parmiggiani, F. A refined gamma MAP SAR speckle filter with improved geometrical adaptivity. *IEEE Trans. Geosci. Remote Sens.* **1995**, *33*, 1245–1257. [CrossRef]
65. Perona, P.; Malik, J. Scale-space and edge detection using anisotropic diffusion. *IEEE Trans. Pattern Anal. Mach. Intell.* **1990**, *12*, 629–639. [CrossRef]
66. Lee, J.S. Digital image smoothing and the sigma filter. *Comput. Vis. Graph. Image Process.* **1983**, *24*, 255–269. [CrossRef]
67. Lee, J.S.; Wen, J.H.; Ainsworth, T.L.; Chen, K.S.; Chen, A.J. Improved Sigma Filter for Speckle Filtering of SAR Imagery. *IEEE Trans. Geosci. Remote Sens.* **2009**, *47*, 202–213. [CrossRef]
68. Argenti, F.; Lapini, A.; Bianchi, T.; Alparone, L. A Tutorial on Speckle Reduction in Synthetic Aperture Radar Images. *IEEE Geosci. Remote Sens. Mag.* **2013**, *1*, 6–35. [CrossRef]
69. Singh, P.; Diwakar, M.; Shankar, A.; Pandey, R.S.; Kumar, M. A Review on SAR Image and its Despeckling. *Arch. Comput. Methods Eng.* **2021**, *28*, 4634–4653. [CrossRef]
70. Baraha, S.; Sahoo, A.K.; Modalavalasa, S. A systematic review on recent developments in nonlocal and variational methods for SAR image despeckling. *Signal Process.* **2022**, *196*, 108521. [CrossRef]
71. Hummel, R.; Moniot, R. Reconstructions from zero crossings in scale space. *IEEE Trans. Acoust. Speech Signal Process.* **1989**, *37*, 2111–2130. [CrossRef]
72. Koenderink, J. The structure of images. *Biol. Cybern.* **1984**, *50*, 363–370. [CrossRef] [PubMed]
73. Black, M.; Sapiro, G.; Marimont, D.; Heeger, D. Robust anisotropic diffusion. *IEEE Trans. Image Process.* **1998**, *7*, 421–432. [CrossRef] [PubMed]

74. Guo, Z.; Wu, L.; Huang, Y.; Guo, Z.; Zhao, J.; Li, N. Water-Body Segmentation for SAR Images: Past, Current, and Future. *Remote Sens.* **2022**, *14*, 1752. [CrossRef]
75. Canny, J. A Computational Approach to Edge Detection. *IEEE Trans. Pattern Anal. Mach. Intell.* **1986**, *PAMI-8*, 679–698. [CrossRef]
76. Otsu, N. A threshold selection method from gray level histograms. *IEEE Trans. Syst. Man Cybern.* **1979**, *9*, 62–66. [CrossRef]
77. Kheradmandi, N.; Mehranfar, V. A critical review and comparative study on image segmentation-based techniques for pavement crack detection. *Constr. Build. Mater.* **2022**, *321*, 126162. [CrossRef]
78. Tockner, K.; Ward, J.V.; Arscott, D.B.; Edwards, P.J.; Kollmann, J.; Gurnell, A.M.; Petts, G.E.; Maiolini, B. The Tagliamento River: A model ecosystem of European importance. *Aquat. Sci.* **2003**, *65*, 239–253. [CrossRef]
79. Tarquini, S.; Isola, I.; Favalli, M.; Mazzarini, F.; Bisson, M.; Pareschi, M.; Boschi, E. TINITALY/01: A new triangular irregular network of Italy. *Ann. Geophys.* **2007**, *50*, 407–425. [CrossRef]
80. Vollrath, A.; Mullissa, A.; Reiche, J. Angular-Based Radiometric Slope Correction for Sentinel-1 on Google Earth Engine. *Remote Sens.* **2020**, *12*, 1867. [CrossRef]
81. Doering, M.; Uehlinger, U.; Rotach, A.; Schlaepfer, D.R.; Tockner, K. Ecosystem expansion and contraction dynamics along a large Alpine alluvial corridor (Tagliamento River, Northeast Italy). *Earth Surf. Process. Landf.* **2007**, *32*, 1693–1704. [CrossRef]
82. van der Nat, D.; Schmidt, A.P.; Tockner, K.; Edwards, P.J.; Ward, J.V. Inundation Dynamics in Braided Floodplains: Tagliamento River, Northeast Italy. *Ecosystems* **2002**, *5*, 636–647. [CrossRef]
83. Welber, M.; Bertoldi, W.; Tubino, M. The response of braided planform configuration to flow variations, bed reworking and vegetation: The case of the Tagliamento River, Italy. *Earth Surf. Process. Landf.* **2012**, *37*, 572–582. [CrossRef]
84. Rinaldi, M.; Darby, S.E. 9 Modelling river-bank-erosion processes and mass failure mechanisms: progress towards fully coupled simulations. *Dev. Earth Surf. Process.* **2007**, *11*, 213–239. [CrossRef]
85. Farò, D.; Baumgartner, K.; Vezza, P.; Zolezzi, G. A novel unsupervised method for assessing mesoscale river habitat structure and suitability from 2D hydraulic models in gravel-bed rivers. *Ecohydrology* **2022**, *15*, e2452. [CrossRef]
86. Best, J. Anthropogenic stresses on the world's big rivers. *Nat. Geosci.* **2019**, *12*, 7–21. [CrossRef]
87. Florsheim, J.L.; Mount, J.F.; Chin, A. Bank Erosion as a Desirable Attribute of Rivers. *BioScience* **2008**, *58*, 519–529. [CrossRef]
88. Langhorst, T.; Pavelsky, T. Global Observations of Riverbank Erosion and Accretion From Landsat Imagery. *J. Geophys. Res. Earth Surf.* **2023**, *128*, e2022JF006774. [CrossRef]
89. Boothroyd, R.J.; Williams, R.D.; Hoey, T.B.; Barrett, B.; Prasojo, O.A. Applications of Google Earth Engine in fluvial geomorphology for detecting river channel change. *WIREs Water* **2021**, *8*, e21496. [CrossRef]
90. Bizzi, S.; Demarchi, L.; Grabowski, R.; Weissteiner, C.J.; Van de Bund, W. The use of remote sensing to characterise hydromorphological properties of European rivers. *Aquat. Sci.* **2016**, *78*, 57–70. [CrossRef]
91. Clement, M.; Kilsby, C.; Moore, P. Multi-temporal synthetic aperture radar flood mapping using change detection. *J. Flood Risk Manag.* **2018**, *11*, 152–168. [CrossRef]
92. Wu, X.; Zhang, Z.; Xiong, S.; Zhang, W.; Tang, J.; Li, Z.; An, B.; Li, R. A Near-Real-Time Flood Detection Method Based on Deep Learning and SAR Images. *Remote Sens.* **2023**, *15*, 2046. [CrossRef]
93. Swain, P.; King, R. Two effective feature selection criteria for multispectral remote sensing. In Proceedings of the First International Joint Conference on Pattern Recognition, Mayflower Hotel, Washington, DC, USA, November 1973.
94. Demirkaya, O.; Asyali, M.H. Determination of image bimodality thresholds for different intensity distributions. *Signal Process. Image Commun.* **2004**, *19*, 507–516. [CrossRef]
95. Ashman, K.; Bird, C.M.; Zepf, S.E. Detecting Bimodality in Astronomical Datasets. *arXiv* **1994**, arXiv:astro-ph/9408030. [CrossRef]
96. Hori, M. Near-daily monitoring of surface temperature and channel width of the six largest Arctic rivers from space using GCOM-C/SGLI. *Remote Sens. Environ.* **2021**, *263*, 112538. [CrossRef]
97. Feng, M.; Zolezzi, G.; Pusch, M. Effects of thermopeaking on the thermal response of alpine river systems to heatwaves. *Sci. Total Environ.* **2018**, *612*, 1266–1275. [CrossRef]
98. Swain, R.; Sahoo, B. Improving river water quality monitoring using satellite data products and a genetic algorithm processing approach. *Sustain. Water Qual. Ecol.* **2017**, *9–10*, 88–114. [CrossRef]
99. Intajag, S.; Chitwong, S. Speckle Noise Estimation with Generalized Gamma Distribution. In Proceedings of the 2006 SICE-ICASE International Joint Conference, Busan, Republic of Korea, 18–21 October 2006; pp. 1164–1167. [CrossRef]
100. Escamilla, H.M.; Méndez, E.R. Speckle statistics from gamma-distributed random-phase screens. *J. Opt. Soc. Am. A-Opt. Image Sci. Vis.* **1991**, *8*, 1929–1935. [CrossRef]
101. Giustarini, L.; Vernieuwe, H.; Verwaeren, J.; Chini, M.; Hostache, R.; Matgen, P.; Verhoest, N.; De Baets, B. Accounting for image uncertainty in SAR-based flood mapping. *Int. J. Appl. Earth Obs. Geoinf.* **2015**, *34*, 70–77. [CrossRef]
102. Chehibi, M.; Ferchichi, A.; Farah, I.R. Representing and modeling spatio-temporal uncertainty using belief function theory in flood extent mapping. *Expert Syst. Appl.* **2022**, *209*, 118212. [CrossRef]
103. Giustarini, L.; Hostache, R.; Matgen, P.; Schumann, G.J.P.; Bates, P.D.; Mason, D.C. A Change Detection Approach to Flood Mapping in Urban Areas Using TerraSAR-X. *IEEE Trans. Geosci. Remote Sens.* **2013**, *51*, 2417–2430. [CrossRef]

104. Chapman, B.; McDonald, K.; Shimada, M.; Rosenqvist, A.; Schroeder, R.; Hess, L. Mapping Regional Inundation with Spaceborne L-Band SAR. *Remote Sens.* **2015**, *7*, 5440–5470. [CrossRef]
105. Pierdicca, N.; Chini, M.; Pulvirenti, L. Enhanced Land Cover and Flood Mapping at C- and L-BAND. In Proceedings of the IGARSS 2020—2020 IEEE International Geoscience and Remote Sensing Symposium, Waikoloa, HI, USA, 26 September–2 October 2020; pp. 4061–4064. [CrossRef]